Electronic Research Archive

https://www.aimspress.com/journal/era

ERA, 33(6): 3431–3449
DOI: 10.3934/era.2025152
Received: 10 March 2025
Revised: 15 May 2025
Accepted: 29 May 2025
Published: 03 June 2025

Research article

Nonconvex high-order TV and ℓ_0 norm-based method for image restoration

Ben Wang[1,*] **and Zijie Lan**[2]

[1] School of Mathematics and Statistics, Hunan University of Science and Technology, Xiangtan 411201, China

[2] School of Mathematical Sciences, Guangxi Minzu University, Nanning 530006, China

* **Correspondence:** Email: bwangzg@163.com.

Abstract: In order to obtain high-quality restoration outcomes, this paper proposed a new nonconvex variational model tailored for reconstructing blurred images corrupted by impulse noise. The newly designed optimization framework integrated nonconvex high-order total variation regularization with ℓ_0 norm data fidelity. This combination aided in overcoming the staircase artifacts and maintaining sharp contours while tackling the poor performance of ℓ_1 norm-based data fidelity in handling high-density impulse noise. To deal with the nonconvex optimization problem, we designed an efficient alternating direction method of multipliers by combining the variable splitting technique with the iteratively reweighted ℓ_1 algorithm. Finally, numerous experiments demonstrated that the suggested scheme achieves competitive performance in terms of objective metrics and visual quality.

Keywords: image restoration; impulse noise; nonconvex function; ℓ_0 norm; alternating direction method of multipliers

1. Introduction

For a long time, image restoration has been regarded as a fundamental yet challenging topic in the field of image processing. In numerous applications, it remains of significant importance as a crucial preprocessing step. Among them, restoring images corrupted by impulse noise and blur has become a prominent research direction. Impulse noise typically arises from electromagnetic interference, sensor inaccuracies, or imperfections in communication systems [1]. This type of noise generally manifests in two primary forms: salt-and-pepper noise and random-valued impulse noise. Both variants degrade image quality by altering the values of a randomly selected subset of pixels while leaving the remaining pixels unaffected [2]. As a consequence, developing effective methods to remove impulse noise and blur is of significant importance.

In the field of variational methods for image restoration, the total variation (TV) regularization

method, originally developed by Rudin et al. [3], has been proven effective in preserving edge details. Although the ℓ_2 norm data fitting used in their work demonstrates significant efficacy in removing Gaussian noise, its susceptibility to outliers often leads to artifacts during impulse noise removal. To better address this task, the studies [4, 5] present an improved variational model, which combines the TV regularization with ℓ_1 norm fidelity, achieving better performance in impulse noise removal.

The TV-based method excels at preserving image gradient sparsity and sharp edge details. However, it potentially assumes that images consist of piecewise constant regions, which may lead to undesirable staircase artifacts in the recovered results. In response to this constraint, researchers have developed various improved solvers. Notable methods include the high-order TV (HOTV) [6–8] and the total generalized variation (TGV) models [9, 10], which utilize high-order derivatives to enhance their performance. Extensive research has shown that the techniques based on high-order derivatives can suppress the staircase artifacts, but their inherent diffusion properties often result in blurred edges. Besides, there are many other related improved methods, as shown in the references [11–13].

As demonstrated in the studies [14, 15], nonconvex potential functions exhibit distinct advantages in preserving sharp edges. This has prompted extensive research into nonconvex potential functions by numerous authors, aiming to achieve superior image restoration. For example, the works [16–18] have incorporated nonconvex potential functions into the TV regularizer, leading to the modified nonconvex TV (NTV) variants with improved performance. However, it can be observed that the staircase effect in NTV is more pronounced than in the TV-based methods. To better preserve edges while mitigating the staircase effect, nonconvex HOTV (NHOTV) [19–21], nonconvex fractional-order TV [22], and nonconvex TGV [23–25] models have been developed recently.

The aforementioned image restoration approaches are primarily designed based on the ℓ_1 norm. Although they are effective for noise removal, the ℓ_1 norm often yields over-penalized reconstruction results [26]. Moreover, their performance significantly deteriorates under the high-intensity impulse noise cases, frequently resulting in image distortion. To address these limitations, Yuan et al. [27] proposed an ℓ_0TV model that incorporates the ℓ_0 norm fidelity, which demonstrates superior impulse noise removal while preserving image details. However, the TV regularization inevitably introduces the staircase artifacts in the reconstructed images.

To achieve high-quality image restoration, this study proposes a novel nonconvex optimization model. The developed new model combines the advantages of the NHOTV regularizer and ℓ_0 norm fidelity, which can reduce the staircase artifacts while preserving edge details and improve the reconstruction accuracy for images corrupted by impulse noise.

The main contributions of this study are threefold. First, by incorporating a nonconvex ℓ_p function into the HOTV penalty, we propose a novel regularizer. This regularizer, combined with the ℓ_0 norm fidelity term, forms a new nonconvex model for image restoration under impulse noise. Second, to solve this optimization problem, we develop an adjusted alternating direction method of multipliers by integrating the iteratively reweighted ℓ_1 algorithm with the variable splitting technique. Finally, numerical experiments demonstrate that the proposed scheme outperforms some existing restoration methods in terms of both visual quality and objective evaluation metrics.

The remainder of this paper is organized as follows. Section 2 introduces the detailed formulation of the proposed model. In Section 3, we have derived the solution process for each subproblem in detail. Section 4 demonstrates the effectiveness of our approach through comprehensive numerical experiments. Finally, Section 5 concludes the paper by summarizing our findings.

2. Proposed model

As mentioned in the reference [27], the image restoration model based on TV regularization and ℓ_0 Norm fidelity can be expressed as

$$\min_u \mathrm{TV}(u) + \lambda \|o \odot |Ku - f|\|_0, \tag{1}$$

where $\mathrm{TV}(u) = \|\nabla u\|_1$ represents the TV regularization term, $\lambda > 0$ is the weighting parameter, $o \in \{0,1\}^n$ with $n = n_1 \times n_2$ (the total number of pixels) is specified by the user. When $o_i = 0$, it indicates the pixel in position i is an outlier, while when $o_i = 1$, it indicates the pixel in position i is a potential outlier. In this paper, $o_i = 0$ when $b_i = u_{max}$ or $b_i = u_{min}$, and otherwise $o_i = 1$ for the salt-and-pepper impulse noise. $\odot$ stands for element-wise multiplication, $K \in \mathbb{R}^{n\times n}$ is a linear blurring operator, u and f represent the normalized original image and the observed image, respectively, and $\|\cdot\|_0$ denotes the number of non-zero elements in a vector.

To improve the quality of image restoration, this paper introduces a nonconvex ℓ_p function into the HOTV and proposes an image restoration model based on NHOTV penalty and ℓ_0 norm fidelity. Specifically, the established mathematical model is

$$\min_u \|\nabla^2 u\|_p^p + \lambda \|o \odot |Ku - f|\|_0, \tag{2}$$

where $0 < p < 1$, and $\|v\|_p^p = \sum_{i=1}^n |v_i|^p$. The second-order gradient operator ∇^2 is defined as

$$\nabla^2 u = \begin{pmatrix} u_{xx} & u_{xy} \\ u_{yx} & u_{yy} \end{pmatrix}, \quad |\nabla^2 u| = \sqrt{u_{xx}^2 + u_{xy}^2 + u_{yx}^2 + u_{yy}^2}.$$

When $p = 1$, model (2) degenerates into the classic second-order TV model. Therefore, the proposed nonconvex high-order penalty term combines the merits of both HOTV and nonconvex functions, enabling it to overcome the staircasing effect while preserving edge details of images.

To support efficient numerical computations, for an image with dimensions of $n_1 \times n_2$ pixels, the discrete second-order gradient operator is defined as

$$(\nabla^2 u)_{i,j} = \begin{bmatrix} D_x^-(D_x^+ u)_{i,j} & D_x^+(D_y^+ u)_{i,j} \\ D_y^+(D_x^+ u)_{i,j} & D_y^-(D_y^+ u)_{i,j} \end{bmatrix},$$

where the forward and backward finite difference operators are respectively defined as

$$(D_x^+ u)_{i,j} = \begin{cases} u_{i,j+1} - u_{i,j}, & 1 \le j < n_2, \\ u_{i,1} - u_{i,n_2}, & j = n_2, \end{cases} \quad (D_y^+ u)_{i,j} = \begin{cases} u_{i+1,j} - u_{i,j}, & 1 \le i < n_1, \\ u_{1,j} - u_{n_1,j}, & i = n_1, \end{cases}$$

$$(D_x^- u)_{i,j} = \begin{cases} u_{i,1} - u_{i,n_2}, & j = 1, \\ u_{i,j} - u_{i,j-1}, & 1 < j \le n_2, \end{cases} \quad (D_y^- u)_{i,j} = \begin{cases} u_{1,j} - u_{n_1,j}, & i = 1, \\ u_{i,j} - u_{i-1,j}, & 1 < i \le n_1. \end{cases}$$

where the relationship $D_x^+(D_y^+ u)_{i,j} = D_y^-(D_x^- u)_{i,j}$ holds. Note that the adjoint of ∇^2, denoted by $(\nabla^2)^T$, satisfies the equality $\langle u, \mathrm{div}^2 p\rangle_X = \langle \nabla^2 u, p\rangle_Y$, where X denotes the Euclidean space $\mathbb{R}^{n_1\times n_2}$ and Y represents the matrix space $\mathbb{R}^{n_1\times n_2} \times \mathbb{R}^{n_1\times n_2} \times \mathbb{R}^{n_1\times n_2} \times \mathbb{R}^{n_1\times n_2}$. Moreover, the second-order divergence operator can be expressed as

$$(\mathrm{div}^2 p)_{i,j} = D_x^+(D_x^- p)_{i,j} + D_x^-(D_y^- p)_{i,j} + D_y^-(D_x^- p)_{i,j} + D_y^+(D_y^- p)_{i,j}.$$

3. Optimization algorithm

To solve the nonconvex model (2), we first present an important property of the ℓ_0 norm. According to the work [26], for $\forall \vartheta \in \mathbb{R}^n$, the ℓ_0 norm possesses the following variational characteristic:

$$\|\vartheta\|_0 = \min_{0\le z\le 1} \langle 1, 1-z\rangle, \quad \text{s.t. } z \odot |\vartheta| = 0. \tag{3}$$

Furthermore, $\tilde{z} = 1 - \text{sgn}(|\vartheta|)$ is the unique optimal solution to problem (3), with sgn being the sign function. Leveraging this property, the proposed new model can be transformed into the following easily solvable constrained optimization problem

$$\min_{u,0\le z\le 1} \|\nabla^2 u\|_p^p + \lambda\langle 1, 1-z\rangle, \text{ s.t. } z \odot o \odot |Ku - f| = 0. \tag{4}$$

By utilizing the variable splitting technique and introducing two auxiliary variables, d and v, the optimization problem (4) can be transformed into

$$\min_{u,d,v,0\le z\le 1} \|d\|_p^p + \lambda\langle 1, 1-z\rangle, \text{ s.t. } \nabla^2 u = d,\ Ku - f = v,\ z \odot o \odot |v| = 0. \tag{5}$$

For the aforementioned constrained optimization problem, we employ the alternating direction method of multipliers (ADMM) to find the solution. As a consequence, this leads to the following iterative algorithm

$$\begin{aligned}(u^{k+1}, d^{k+1}, v^{k+1}, z^{k+1}) = \arg\min_{u,d,v,0\le z\le 1} &\|d\|_p^p + \lambda\langle 1, 1-z\rangle + \langle \nabla^2 u - d, \beta^k\rangle + \frac{\gamma_1}{2}\|\nabla^2 u - d\|_2^2 \\ &+ \langle Ku - f - v, \delta^k\rangle + \frac{\gamma_2}{2}\|Ku - f - v\|_2^2 \\ &+ \langle z \odot o \odot |v|, \xi^k\rangle + \frac{\gamma_3}{2}\|z \odot o \odot |v|\|_2^2,\end{aligned} \tag{6}$$

Note that in expression (6), $\gamma_1, \gamma_2, \gamma_3 > 0$ are three penalty parameters. In addition, the update formula for the Lagrange multipliers is

$$\begin{cases}\beta^{k+1} = \beta^k + \gamma_1(\nabla^2 u^{k+1} - d^{k+1}),\\ \delta^{k+1} = \delta^k + \gamma_2(Ku^{k+1} - f - v^{k+1}),\\ \xi^{k+1} = \xi^k + \gamma_3(z^{k+1} \odot o \odot |v^{k+1}|).\end{cases} \tag{7}$$

It should be noted that the four subproblems in problem (6) are all decoupled. Utilizing the idea of alternating minimization, the solutions to the subproblems for the variables u, d, v, and z can be written as the following iterative framework:

$$\begin{cases}u^{k+1} = \arg\min_u \langle \nabla^2 u - d^k, \beta^k\rangle + \frac{\gamma_1}{2}\|\nabla^2 u - d^k\|_2^2 + \langle Ku - f - v^k, \delta^k\rangle \\ \qquad + \frac{\gamma_2}{2}\|Ku - f - v^k\|_2^2,\\ d^{k+1} = \arg\min_d \|d\|_p^p + \langle \nabla^2 u^{k+1} - d, \beta^k\rangle + \frac{\gamma_1}{2}\|\nabla^2 u^{k+1} - d\|_2^2,\\ v^{k+1} = \arg\min_v \langle Ku^{k+1} - f - v, \delta^k\rangle + \frac{\gamma_2}{2}\|Ku^{k+1} - f - v\|_2^2 \\ \qquad + \langle z^k \odot o \odot |v|, \xi^k\rangle + \frac{\gamma_3}{2}\|z^k \odot o \odot |v|\|_2^2,\\ z^{k+1} = \arg\min_{0\le z\le 1} \lambda\langle 1, 1-z\rangle + \langle z \odot o \odot |v^{k+1}|, \xi^k\rangle + \frac{\gamma_3}{2}\|z \odot o \odot |v^{k+1}|\|_2^2.\end{cases} \tag{8}$$

Next, we will solve each subproblem in detail one by one. Firstly, for the u-subproblem, it can be equivalently written as

$$u^{k+1} = \arg\min_{u} \frac{\gamma_1}{2}\left\|\nabla^2 u - d^k + \frac{\beta^k}{\gamma_1}\right\|_2^2 + \frac{\gamma_2}{2}\left\|Ku - f - v^k + \frac{\delta^k}{\gamma_2}\right\|_2^2. \tag{9}$$

Combining its first-order necessary condition for optimality, we can obtain the subdifferential with respect to the variable u and assign $u \to u^{k+1}$, namely,

$$\Big(\gamma_1(\nabla^2)^T\nabla^2 + \gamma_2 K^T K\Big)u^{k+1} = \gamma_1(\nabla^2)^T\Big(d - \frac{\beta^k}{\gamma_1}\Big) + \gamma_2 K^T\Big(f + v - \frac{\delta^k}{\gamma_2}\Big), \tag{10}$$

where Λ^T represents the adjoint operator of Λ. Under periodic boundary conditions, the operators $(\nabla^2)^T\nabla^2$ and $K^T K$ are both block circulant matrices. Therefore, by utilizing the fast Fourier transform and its inverse, the solution to the u-subproblem can be described as

$$u^{k+1} = F^{-1}\Big(\frac{\gamma_1 F(\nabla^2)^* \odot F(d - \frac{\beta^k}{\gamma_1}) + \gamma_2 F(K)^* \odot F(f + v - \frac{\delta^k}{\gamma_2})}{\gamma_1 F(\nabla^2)^* \odot F(\nabla^2) + \gamma_2 F(K)^* \odot F(K)}\Big). \tag{11}$$

In Eq (11), F and F^{-1} represent the fast Fourier transform and its inverse transform, respectively, and $*$ denotes the complex conjugate.

According to the second formula in Eq (8), the d-subproblem can be written as

$$d^{k+1} = \arg\min_{d} \|d\|_p^p + \frac{\gamma_1}{2}\left\|\nabla^2 u^{k+1} - d + \frac{\beta^k}{\gamma_1}\right\|_2^2. \tag{12}$$

Given that Eq (12) involves a nonconvex ℓ_p norm penalty, direct solving is highly challenging. Here, by using the iteratively reweighted ℓ_1 algorithm, the convex approximation of the nonconvex optimization problem (12) can be expressed as

$$d^{k+1} = \arg\min_{d} w^{k+1}\|d\|_1 + \frac{\gamma_1}{2}\left\|d - \Big(\nabla^2 u^{k+1} + \frac{\beta^k}{\gamma_1}\Big)\right\|_2^2, \tag{13}$$

where w represents a positive weighting function, which is determined by the values from the $(k+1)$-th iteration. Its calculation formula is given by

$$w^{k+1} = \frac{p}{(|\nabla^2 u^{k+1}| + \tau)^{1-p}}, \tag{14}$$

where $\tau > 0$ represents a very small positive number, intended to prevent division by zero in the denominator. Subsequently, by using the classical shrinkage operator, the solution to the d-subproblem can be described as

$$d^{k+1} = \text{shrink}\Big(\nabla^2 u^{k+1} + \frac{\beta^k}{\gamma_1}, \frac{w^{k+1}}{\gamma_1}\Big), \tag{15}$$

where shrink denotes the shrinkage operator, defined as $\text{shrink}(t, \eta) = \text{sgn}(t) * \max(\|t\|_2 - \eta, 0)$.

As for the v-subproblem, it can be equivalently written as

$$v^{k+1} = \arg\min_{v} \frac{\gamma_2}{2}\left\|v - \Big(Ku^{k+1} - f + \frac{\delta^k}{\gamma_2}\Big)\right\|_2^2 + \frac{\gamma_3}{2}\left\|z^k \odot o \odot |v| + \frac{\xi^k}{\gamma_3}\right\|_2^2. \tag{16}$$

Let $q^k = Ku^{k+1} - f + \delta^k/\gamma_2$ and $t^k = z^k \odot o$. The above equation can be simplified as

$$v^{k+1} = \arg\min_v \frac{\gamma_2}{2}\|v - q^k\|_2^2 + \frac{\gamma_3}{2}\left\|t^k \odot |v| + \frac{\xi^k}{\gamma_3}\right\|_2^2. \tag{17}$$

By utilizing the generalized shrinkage formula, the solution to the v-subproblem determined by Eq (17) is given by

$$v^{k+1} = \text{shrink}\Big(\frac{\gamma_2 q^k}{\gamma_2 + \gamma_3(t^k)^2}, \frac{t^k \odot \xi^k}{\gamma_2 + \gamma_3(t^k)^2}\Big). \tag{18}$$

Finally, we proceed to solve the z-subproblem. For computational convenience, it is equivalently rewritten as

$$z^{k+1} = \arg\min_{0\le z\le 1} \frac{1}{2}\gamma_3 o \odot v^{k+1} \odot v^{k+1} \odot z^2 + (\xi^k \odot o \odot |v^{k+1}| - \lambda) \odot z. \tag{19}$$

According to the projection formula, we obtain

$$z^{k+1} = \min\Big(1, \max\Big(0, -\frac{\xi^k \odot o \odot |v^{k+1}| - \lambda}{\gamma_3 o \odot v^{k+1} \odot v^{k+1}}\Big)\Big). \tag{20}$$

In summary, by combining the solution processes of each subproblem described above, a modified ADMM framework can be derived as follows.

Algorithm 1. ADMM for image restoration

Input: f and K.
Initialization: $u^0, d^0, v^0, z^0, \beta^0, \delta^0, \xi^0$; **Set**: $\lambda, p, \gamma_1, \gamma_2, \gamma_3$.
while stopping criterion is not met, **do**
    Compute u^{k+1} by (11);
    Compute d^{k+1} by (15);
    Compute v^{k+1} by (18);
    Compute z^{k+1} by (20);
    Update β^{k+1}, δ^{k+1}, and ξ^{k+1} by (7);
end while
Output: $u = u^{k+1}$.

Here, we provide a concise overview of the computational complexity associated with Algorithm 1. The computation of the u-subproblem involves FFT and inverse FFT operations, resulting in a complexity of $O(n_1 n_2 \log(n_1 n_2))$ for an image of dimensions $n_1 \times n_2$. Additionally, it is worth noting that the d-subproblem and v-subproblem are tackled using the shrinkage operator and generalized shrinkage formula, respectively. Their computation costs are both linear with a complexity of $O(n_1 n_2)$. Finally, the z-subproblem is solved using a projection formula, which also costs linear time with $O(n_1 n_2)$.

In what follows, we provide a brief analysis of the convergence properties of the designed algorithm. More precisely, we establish the global convergence of the proposed algorithm by verifying the three key conditions: sufficient decrease condition, relative error condition, and continuity condition of [28] under the Kurdyka–Lojasiewicz (KL) framework.

Theorem 1. The sequence $\{(u^k, d^k, v^k, z^k)\}$ generated by Algorithm 1 satisfies

$$\sum_{k=0}^{\infty}\Big(\|u^{k+1} - u^k\|_2 + \|d^{k+1} - d^k\|_2 + \|v^{k+1} - v^k\|_2 + \|z^{k+1} - z^k\|_2\Big) < \infty,$$

and converges to a critical point of the augmented Lagrangian function $\mathcal{L}$.

Proof. Let $\mathcal{L}(u,d,v,z) = \|d\|_p^p + \lambda\langle 1, 1-z\rangle + \langle \nabla^2 u - d, \beta\rangle + \frac{\gamma_1}{2}\|\nabla^2 u - d\|_2^2 + \langle Ku - f - v, \delta\rangle + \frac{\gamma_2}{2}\|Ku - f - v\|_2^2 + \langle z \odot o \odot |v|, \xi\rangle + \frac{\gamma_3}{2}\|z \odot o \odot |v|\|_2^2$ be the augmented Lagrangian function of problem (5). Since $\mathcal{L}$ is semi-algebraic, and thus it satisfies the KL property [29].

First, for the u-subproblem (9), according to the strong convexity of the quadratic term, we derive that there exists a constant $c_u > 0$ such that $\mathcal{L}(u^{k+1}, d^k, v^k, z^k) \le \mathcal{L}^k - c_u\|u^{k+1} - u^k\|_2^2$ holds. Regarding the d-subproblem (12), by adopting the iteratively reweighted ℓ_1 approximation strategy, the weight update formula (14) ensures that the approximation errors are summable. Thus, there exists $c_d > 0$ such that $\mathcal{L}(u^{k+1}, d^{k+1}, v^k, z^k) \le \mathcal{L}(u^{k+1}, d^k, v^k, z^k) - c_d\|d^{k+1} - d^k\|_2^2$ holds. For the v-subproblem (16), the contraction property of the generalized shrinkage operator guarantees the existence of $c_v > 0$, which satisfies $\mathcal{L}(u^{k+1}, d^{k+1}, v^{k+1}, z^k) \le \mathcal{L}(u^{k+1}, d^{k+1}, v^k, z^k) - c_v\|v^{k+1} - v^k\|_2^2$. For the z-subproblem (19), we have $\mathcal{L}(u^{k+1}, d^{k+1}, v^{k+1}, z^{k+1}) \le \mathcal{L}(u^{k+1}, d^{k+1}, v^{k+1}, z^k) - c_z\|z^{k+1} - z^k\|_2^2$ due to the strong convexity and projection formula. By taking $a = \min\{c_u, c_d, c_v, c_z\}$, we thereby obtain the global descent condition as $\mathcal{L}^{k+1} + a\sum_{t\in\{u,d,v,z\}}\|t^{k+1} - t^k\|_2^2 \le \mathcal{L}^k$.

Second, we bound the subgradients by iteration increments. From the solution to the u-subproblem in the Fourier domain, it yields that there exists a constant $C_u > 0$ such that $\|\partial_u \mathcal{L}^{k+1}\|_2 \le C_u\|u^{k+1} - u^k\|_2$. Due to the characteristics of the shrink operator, we have $\|\partial_d \mathcal{L}^{k+1}\|_2 \le C_d\|d^{k+1} - d^k\|_2$ and $\|\partial_v \mathcal{L}^{k+1}\|_2 \le C_v\|v^{k+1} - v^k\|_2$. By the Lipschitz continuity property of the projection formula (20), we have $\|\partial_z \mathcal{L}^{k+1}\|_2 \le C_z\|z^{k+1} - z^k\|_2$. Furthermore, setting $b = \max\{C_u, C_d, C_v, C_z\}$, we obtain the relative error condition as $\mathrm{dist}(0, \partial\mathcal{L}^{k+1}) \le b\sum_{t\in\{u,d,v,z\}}\|t^{k+1} - t^k\|_2$, where dist is the distance function.

Finally, the coercivity of ℓ_p norm ($0 < p < 1$) and ℓ_0 fidelity and box constraint $z \in [0,1]$ ensure the boundedness of $\{(u^k, d^k, v^k, z^k)\}$. By using Bolzano–Weierstrass theorem, there exists a convergent subsequence $(u^{k_j}, d^{k_j}, v^{k_j}, z^{k_j}) \to (\bar{u}, \bar{d}, \bar{v}, \bar{z})$, This together with the lower semicontinuity of $\mathcal{L}$, ensures that the function value matching at the corresponding limit point, namely, the following continuity condition $\lim_{j\to\infty}\mathcal{L}(u^{k_j}, d^{k_j}, v^{k_j}, z^{k_j}) = \mathcal{L}(\bar{u}, \bar{d}, \bar{v}, \bar{z})$ holds.

By Theorem 2.9 [28], the above three conditions (sufficient decrease, relative error, and continuity) and the KL property of $\mathcal{L}$ imply that the sequence globally converges to a critical point.

4. Experimental results

This section outlines numerous numerical experiments aimed at assessing the efficacy of the newly proposed model for image restoration. For comparative purposes, the introduced method is compared with three related models: TVℓ_1 [5], ℓ_0TV [27], and ℓ_0OGSTV [30] (abbreviated as ℓ_0OTV), which are all solved using the ADMM framework. All experiments are conducted using MATLAB R2023b software on a computer running Windows 10, with 4 GB of RAM and an Intel(R) Core(TM) i5-8250 CPU operating at 1.80 GHz.

In the simulated experiments, we select several standard test images that are widely employed in the field of image processing, including four grayscale images (*House*, *Man*, *Peppers*, *Einstein*) and two color images (*Bird*, *Monarch*), as depicted in Figure 1. To validate the effectiveness of our model, we first conducted pure denoising tests. Next, we evaluated its robustness and adaptability using two different blur types: motion blur with a length of 15 and an angle of 45, and disk blur with a radius of 10. In each deblurring experiment, we further degraded the test images by adding three levels of salt-and-pepper noise (30%, 50% and 70%). This allowed us to assess performance under varying

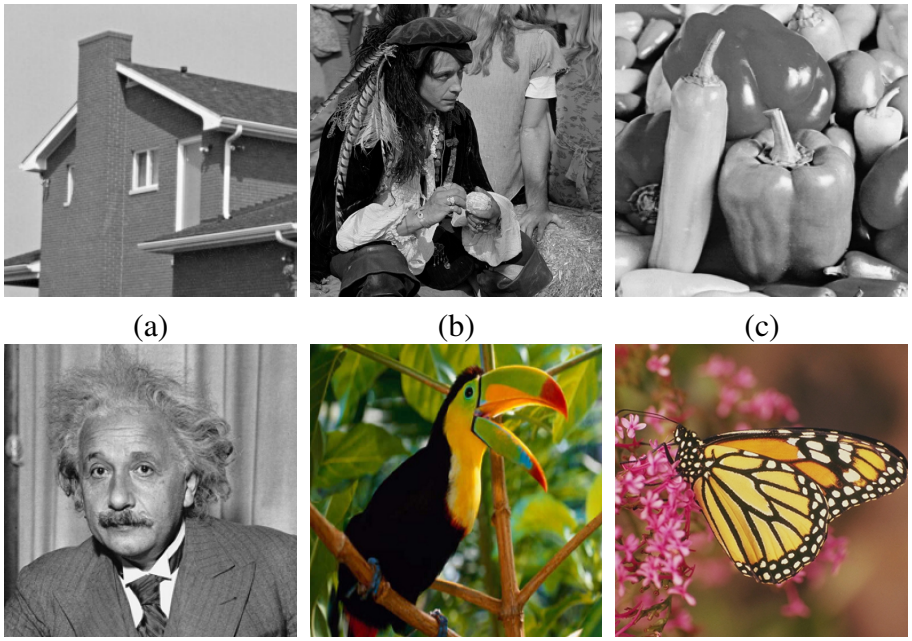

Figure 1. Original test images. (a) House (256 × 256), (b) Man (512 × 512), (c) Peppers (256 × 256), (d) Einstein (256 × 256), (e) Bird (256 × 256), (f) Monarch (360 × 360).

degrees of distortion.

To ensure equitable comparison, the unified stopping criterion for all numerical methods in the experiments is set as

$$\frac{\|u^{k+1} - u^k\|_2}{\|u^k\|_2} < 5 \times 10^{-4}. \tag{21}$$

To enable a clearer and more intuitive comparison of the performance of various methods, we adopt two widely-used metrics: peak signal-to-noise ratio (PSNR) and structural similarity (SSIM), and a modern subjective quality assessment metric: learned perceptual image patch similarity (LPIPS), which serve as three quantitative indicators of image restoration quality. More specifically, the PSNR is defined

Table 1. Quantitative evaluation results on *House* and *Man* images.

Figure	Model	Noise level (10%)					Noise level (20%)					Noise level (30%)				
		Iter	Time	PSNR	SSIM	LPIPS	Iter	Time	PSNR	SSIM	LPIPS	Iter	Time	PSNR	SSIM	LPIPS
House	TVℓ_1	47	0.47	33.6350	0.9275	0.1368	50	0.50	31.5120	0.8854	0.2026	57	0.56	29.8361	0.8446	0.2431
	ℓ_0TV	36	0.32	37.3495	0.9770	0.0442	43	0.36	32.9898	0.9485	0.0703	54	0.42	30.1027	0.9208	0.1248
	ℓ_0OTV	38	0.48	39.2052	0.9818	0.0248	42	0.53	34.0732	0.9578	**0.0453**	45	0.59	31.0431	0.9248	0.1177
	Ours	63	0.73	**40.5528**	**0.9914**	**0.0179**	63	0.81	**35.3425**	**0.9777**	0.0491	64	0.76	**32.1056**	**0.9576**	**0.0924**
Man	TVℓ_1	50	2.34	32,6301	0.9298	0.0880	53	2,71	30.2319	0.8733	0.1461	54	2.96	28.0754	0.7924	0.2369
	ℓ_0TV	38	2.31	33.3991	0.9573	0.0634	47	2.40	30.1472	0.9135	0.1080	58	2.56	27.9136	0.8702	0.1557
	ℓ_0OTV	40	3.89	35.0881	0.9694	0.0603	42	4.98	32.3171	0.9404	0.0734	46	5.02	30.2817	0.9047	0.1134
	Ours	71	5.61	**36.6663**	**0.9833**	**0.0488**	73	4.83	**33.9404**	**0.9670**	**0.0697**	72	5.14	**31.2111**	**0.9413**	**0.1096**

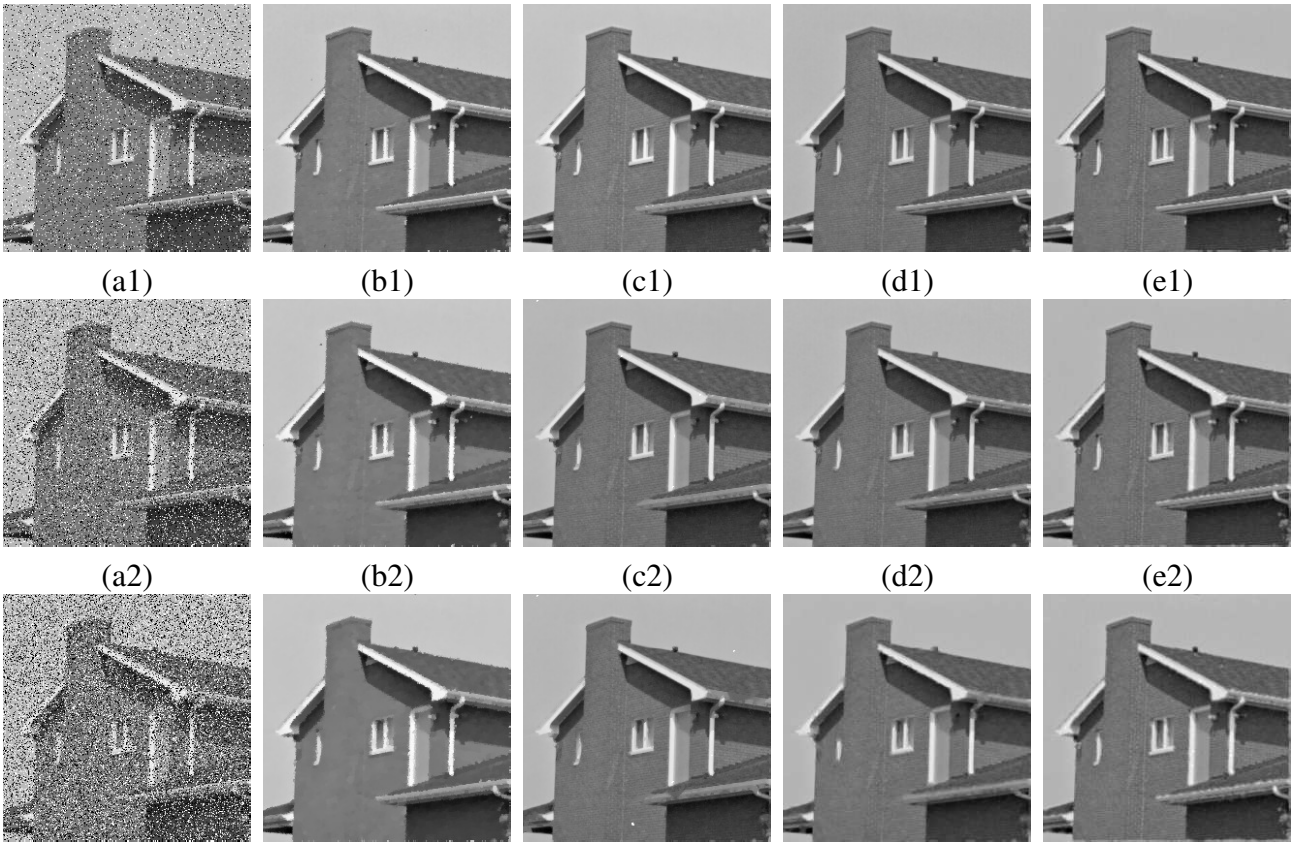

Figure 2. The pure denoising outcomes of different approaches on *House* image. (a1)–(a3) Degraded images, (b1)–(b3) TVℓ_1, (c1)–(c3) ℓ_0TV, (d1)–(d3) ℓ_0OTV, (e1)–(e3) our method.

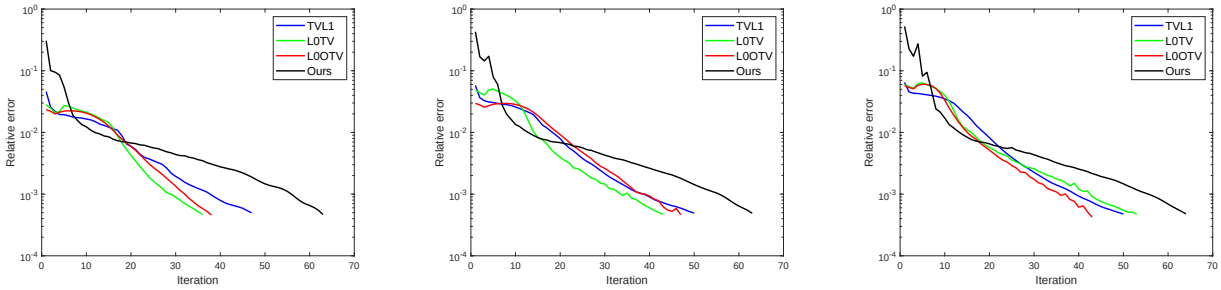

Figure 3. Relationships between relative error and iterations for all methods on *House* image at three noise levels. (a) Level of 10%, (b) level of 20%, (c) level of 30%.

as follows

$$\text{PSNR} = 10\log_{10}\left(\frac{\text{Max}^2 \cdot n_1 n_2}{\|u - \tilde{u}\|_2^2}\right), \tag{22}$$

where u and $\tilde{u}$ represent the original clean image and the restored version, respectively, and Max denotes

Figure 4. The pure denoising outcomes of different approaches on *Man* image. (a1)–(a3) Degraded images, (b1)–(b3) TVℓ_1, (c1)–(c3) ℓ_0TV, (d1)–(d3) ℓ_0OTV, (e1)–(e3) our method.

the maximum pixel value. Furthermore, the SSIM is formulated as follows:

$$\text{SSIM} = \frac{(2\mu_u\mu_{\tilde{u}} + c_1)(2\sigma_{u\tilde{u}} + c_2)}{(\mu_u^2 + \mu_{\tilde{u}}^2 + c_1)(\sigma_u^2 + \sigma_{\tilde{u}}^2 + c_2)}, \tag{23}$$

where μ_u and $\mu_{\tilde{u}}$ are the means of the original and restored images, σ_u and $\sigma_{\tilde{u}}$ are their respective variances, and $c_1, c_2 > 0$ denote two constants. Moreover, $\sigma_{u\tilde{u}}$ is the covariance of u and $\tilde{u}$. Note that higher PSNR and SSIM values correspond to better image restoration quality. Conversely, a lower LPIPS value indicates that the two images are more perceptually similar from the human visual perspective.

4.1. Parameter selection

In this subsection, we focus on discussing the parameter settings for our developed algorithm. Namely, five parameters $\gamma_1, \gamma_2, \gamma_3, \lambda$, and p, involved in model (2) need to be taken into account.

Experimental results demonstrate that the parameters γ_1, γ_3, and p have relatively limited influence on restoration performance. Therefore, to streamline parameter configuration and ensure algorithm stability, we assign fixed values to these parameters. Specifically, we set γ_1 to 5000 for image denoising tasks and 2000 for joint image denoising and deblurring tasks, with $\gamma_3 = 500$ and $p = 0.9$ being uniformly adopted across all configurations. This strategy allows us to achieve consistent restoration quality while focusing on optimizing other more influential parameters.

Table 2. Quantitative evaluation results on *Peppers* and *Einstein* images.

Figure	Model	Noise level (30%)					Noise level (50%)					Noise level (70%)				
		Iter	Time	PSNR	SSIM	LPIPS	Iter	Time	PSNR	SSIM	LPIPS	Iter	Time	PSNR	SSIM	LPIPS
Peppers	TVℓ_1	82	0.82	32.0103	0.9174	0.0712	65	0.61	28.5368	0.8731	0.1406	64	0.59	24.1065	0.7618	0.2573
	ℓ_0TV	108	1.47	34.9937	0.9485	0.0383	112	1.52	32.0728	0.9182	0.0680	140	1.64	29.5206	0.8849	0.1155
	ℓ_0OTV	70	1.26	35.0728	0.9509	0.0683	108	1.75	33.0414	0.9382	0.1016	244	3.71	29.6258	0.9103	0.1395
	Ours	74	1.21	**37.1069**	**0.9713**	**0.0311**	78	1.27	**34.3640**	**0.9502**	**0.0585**	127	2.10	**31.7865**	**0.9179**	**0.1102**
Einstein	TVℓ_1	101	0.91	32.4040	0.8394	0.1388	78	0.80	29.5467	0.7567	0.2500	74	1.16	26.5724	0.6600	0.3749
	ℓ_0TV	114	1.45	34.0789	0.8759	0.1229	119	1.48	31.8598	0.8168	0.1793	141	1.59	30.2060	0.7651	0.2294
	ℓ_0OTV	61	1.08	33.6157	0.8666	0.1651	122	1.81	33.0590	0.8552	0.1748	258	3.90	31.1250	0.8246	0.1848
	Ours	64	1.21	**35.9012**	**0.9302**	**0.0777**	77	1.45	**34.5785**	**0.9120**	**0.0926**	123	2.31	**32.3163**	**0.8664**	**0.1480**

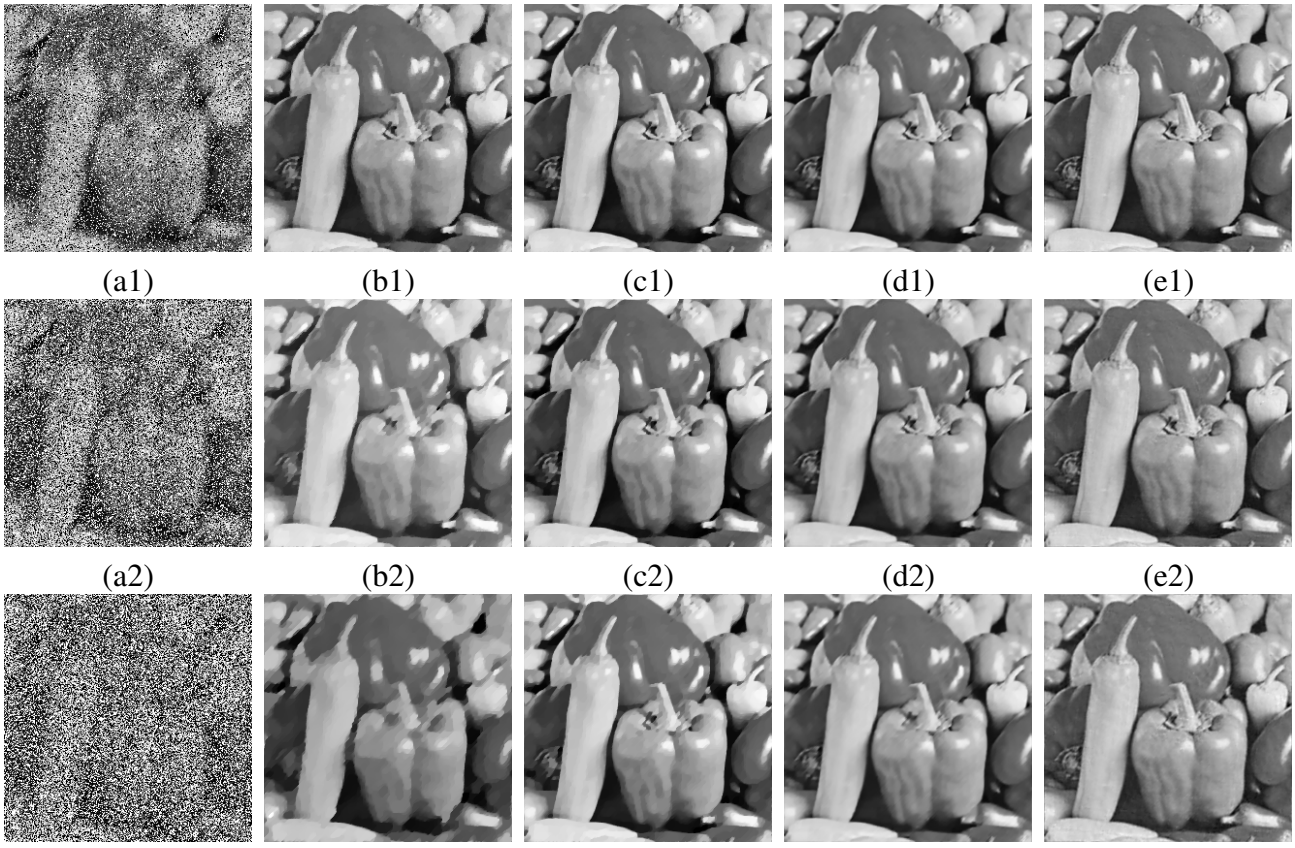

Figure 5. Motion deblurring and denoising results by different methods on *Peppers* image. (a1)–(a3) Degraded images, (b1)–(b3) TVℓ_1, (c1)–(c3) ℓ_0TV, (d1)–(d3) ℓ_0OTV, (e1)–(e3) our method.

The regularization parameter λ and the penalty parameter γ_2 have a significant impact on the experimental results. More precisely, λ plays a key role in noise filtering, while γ_2 directly affects the restoration performance and the convergence speed of the algorithm. The specific values of λ and γ_2 depend on image characteristics, noise levels, and blur types. To achieve optimal restoration results, the regularization parameter λ is tested using the set $\{25, 40, 45, 50, 100, 140, 220\}$ and the penalty parameter γ_2 is selected from the set $\{400, 500, 600, 1200, 1400, 100,000, 110,000, 120,000\}$.

Note that in the designed algorithm, identical parameter settings are applied to all images degraded

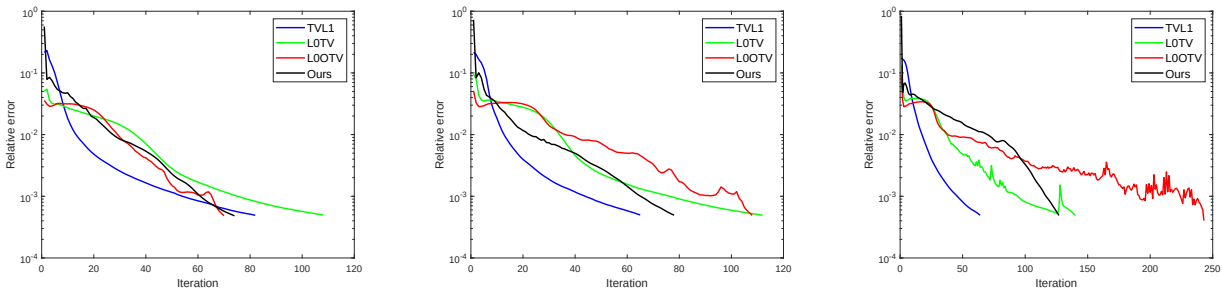

(a) (b) (c)

Figure 6. Relationships between relative error and iterations for all methods on *Peppers* image at three noise levels. (a) Level of 30%, (b) level of 50%, (c) level of 70%.

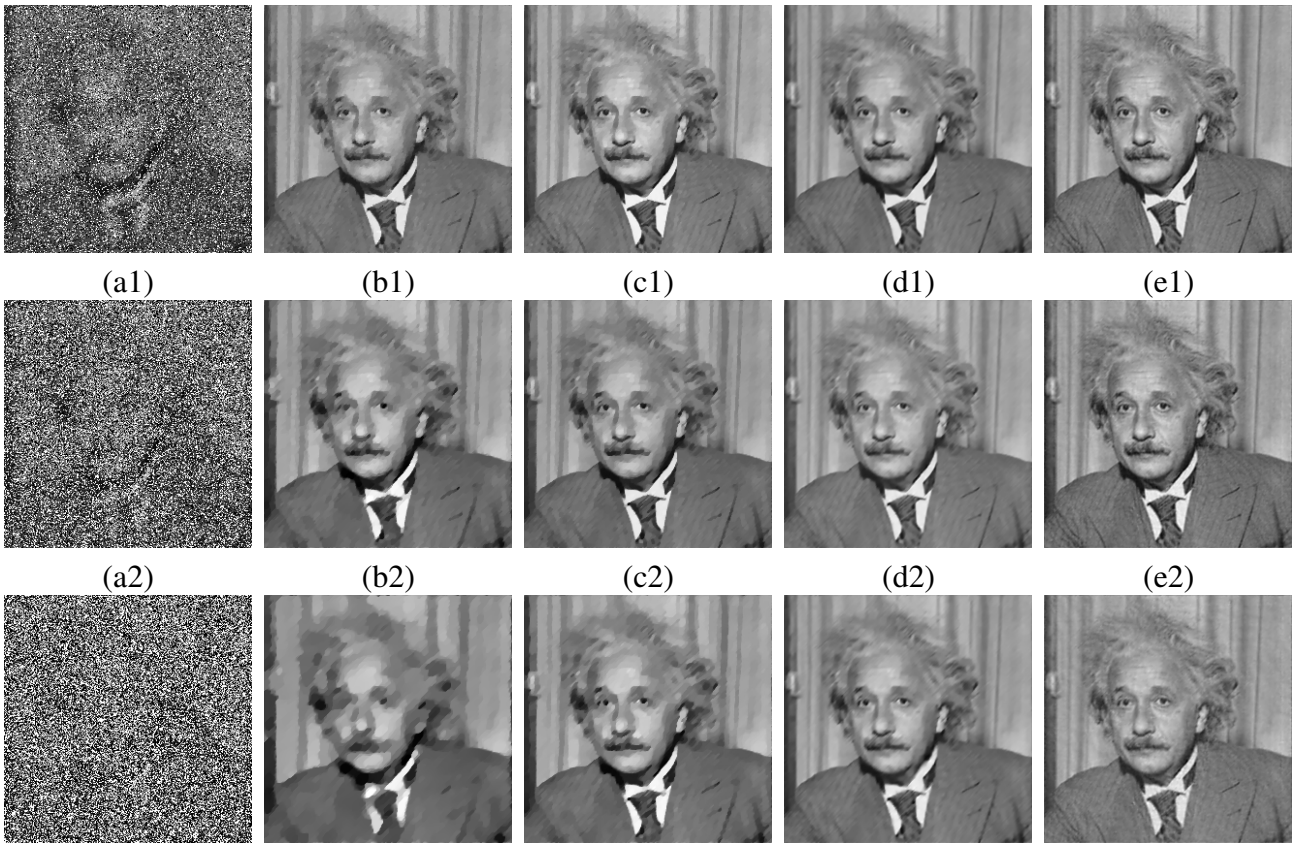

(a1) (b1) (c1) (d1) (e1)

(a2) (b2) (c2) (d2) (e2)

(a3) (b3) (c3) (d3) (e3)

Figure 7. Motion deblurring and denoising results by different methods on *Einstein* image. (a1)–(a3) Degraded images, (b1)–(b3) TVℓ_1, (c1)–(c3) ℓ_0TV, (d1)–(d3) ℓ_0OTV, (e1)–(e3) our method.

by the same type and level of blur and noise. Regarding the determination of these parameters for our comparative models, we have adopted a manual tuning approach, aiming to achieve the preset minimum relative error while simultaneously maximizing the PSNR and SSIM values. Meanwhile, we strive to minimize the number of iterations and reduce the CPU time.

Table 3. Quantitative evaluation results on *Bird* and *Monarch* images.

Figure	Model	Noise level (30%)					Noise level (50%)					Noise level (70%)				
		Iter	Time	PSNR	SSIM	LPIPS	Iter	Time	PSNR	SSIM	LPIPS	Iter	Time	PSNR	SSIM	LPIPS
Bird	TVℓ_1	127	11.10	28.3599	0.8359	0.0893	119	8.22	27.2765	0.8061	0.1123	93	6.20	25.0749	0.7328	0.1713
	ℓ_0TV	206	8.90	30.6692	0.8925	0.0615	213	9.04	29.3577	0.8654	0.0724	268	11.50	27.2654	0.8071	0.1032
	ℓ_0OTV	142	11.60	31.5742	0.9071	0.0993	164	20.54	31.2876	0.9001	0.1064	281	22.86	28.1858	0.8325	0.1684
	Ours	134	9.68	**33.7311**	**0.9549**	**0.0579**	147	10.65	**33.3500**	**0.9512**	**0.0640**	296	21.52	**32.1366**	**0.9179**	**0.0823**
Monarch	TVℓ_1	141	22.28	26.7625	0.8823	0.1051	117	20.24	25.1302	0.8494	0.1304	91	13.40	22.3087	0.7713	0.1914
	ℓ_0TV	191	16.33	28.2254	0.9051	**0.0963**	205	17.42	26.9361	0.8826	**0.1116**	250	21.28	24.7950	0.8364	**0.1416**
	ℓ_0OTV	142	28.05	27.6660	0.9086	0.1490	162	27.36	26.2249	0.8803	0.1787	193	32.11	24.3332	0.8348	0.2266
	Ours	133	19.24	**29.1173**	**0.9422**	0.1120	161	23.20	**28.7980**	**0.9373**	0.1236	129	18.60	**26.6280**	**0.9043**	0.1678

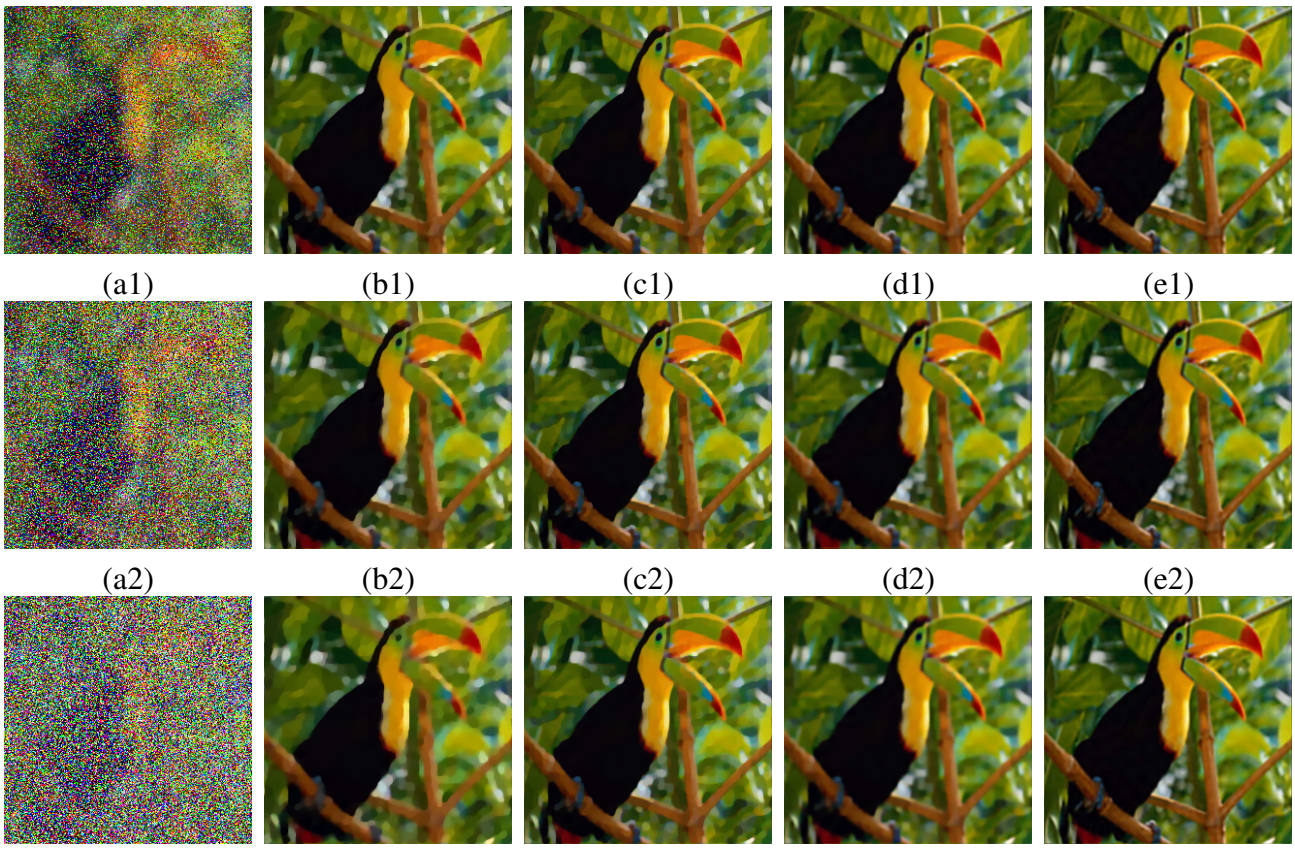

Figure 8. Disk deblurring and denoising results of different methods on *Bird* image. (a1)–(a3) Degraded images, (b1)–(b3) TVℓ_1, (c1)–(c3) ℓ_0TV, (d1)–(d3) ℓ_0OTV, (e1)–(e3) our method.

4.2. Salt-and-pepper noise removal in grayscale images

To validate the effectiveness of the proposed model, we first conducted denoising experiments on the *House* and *Man* test images by adding salt-and-pepper noise at three different intensities: 10%, 20%, and 30%. Figures 2 and 4 present the comparisons of denoising results obtained by TVℓ_1, ℓ_0TV and ℓ_0OTV, and our proposed method on the noisy images. The parameters used in our method remain consistent with the previously described settings. Additionally, Table 1 summarizes the quantitative evaluation metrics, including the number of iterations, CPU time (in seconds), PSNR, SSIM, and

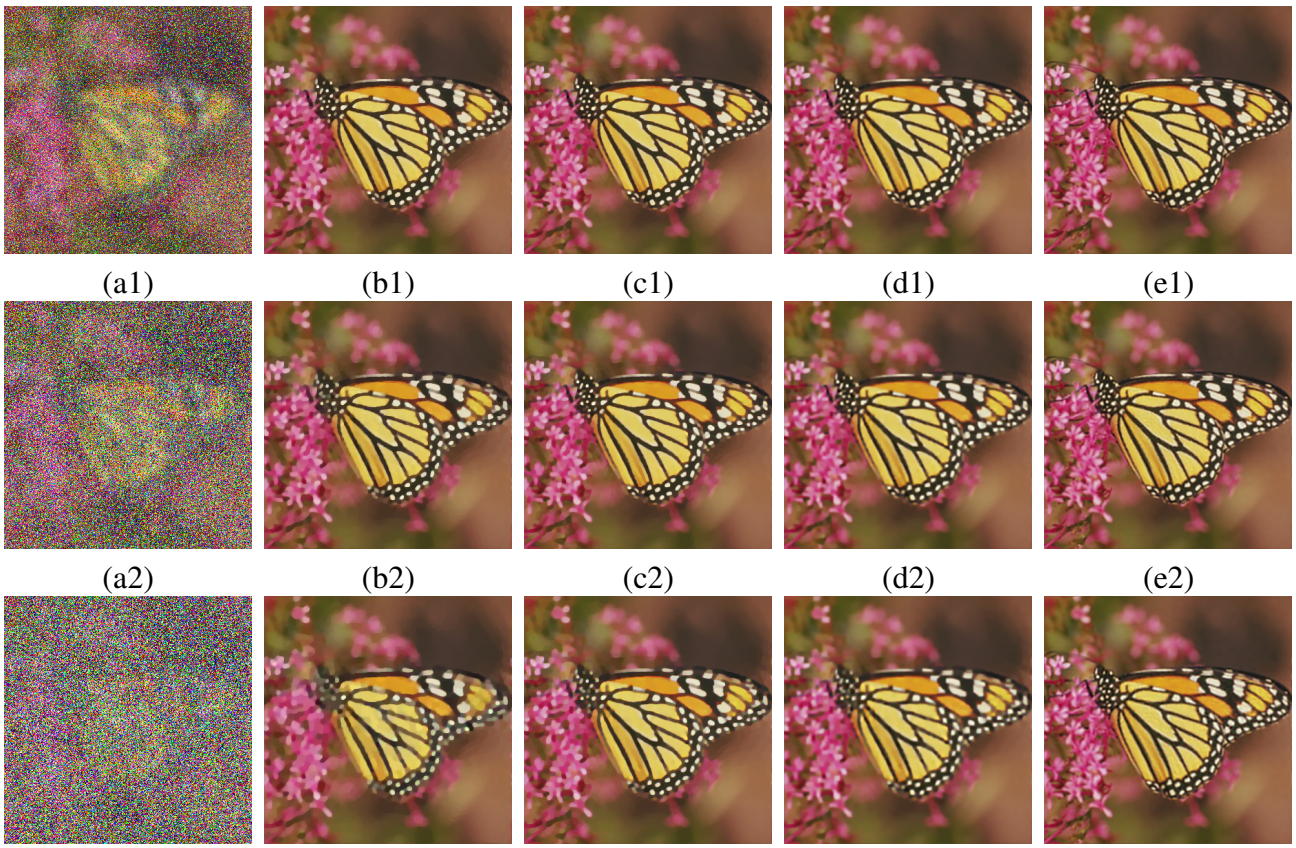

Figure 9. Disk deblurring and denoising results of different methods on *Monarch* image. (a1)–(a3) Degraded images, (b1)–(b3) TVℓ_1, (c1)–(c3) ℓ_0TV, (d1)–(d3) ℓ_0OTV, (e1)–(e3) our method.

LPIPS values, to facilitate a comprehensive comparative analysis. Figure 3 demonstrates the numerical convergence characteristics of all compared methods, as evaluated through the relative errors.

The experimental results demonstrate that all four methods exhibit good denoising performance, but with notable differences. Traditional TV methods (including TVℓ_1 and ℓ_0TV) produce noticeable staircase artifacts in smooth image regions, which stem from the inherent theoretical limitations of the TV regularization term. While the ℓ_0OTV method shows some improvement in reducing the staircase artifacts, its performance enhancement remains limited. In contrast, our proposed method achieves the optimal reconstruction quality, effectively preserving both edge sharpness and texture details. This superiority is further confirmed by the quantitative evaluation results in Table 1, where all objective metrics consistently validate the effectiveness of our model.

4.3. Salt-and-pepper noise and blur removal in grayscale images

To validate the visual performance and generalization capability of the proposed model, some experiments are conducted in this subsection by adding noise and blur. Figures 5 and 7 present the degraded and restored results obtained by four different methods on the test images. Specifically, the experiments include the *Peppers* and *Einstein* images degraded by motion blur and noise. Note that to

achieve satisfactory restoration results, all parameters in our proposed method are set within the ranges described previously. Furthermore, Table 2 summarizes the quantitative evaluation metrics. Figure 6 illustrates the relationship between relative error and iteration count, demonstrating the stability and convergence of the proposed algorithm in the simulation experiments.

The experimental results in Table 2 demonstrate that the proposed model outperforms TVℓ_1, ℓ_0TV, and ℓ_0OTV, as evidenced by higher PSNR and SSIM values and lower LPIPS values. As the intensity of salt-and-pepper noise increases, all tested methods exhibit a gradual decline in PSNR and SSIM metrics. Obviously, even under extreme conditions with 70% pixel corruption, the proposed approach maintains robust performance, consistently surpassing other methods in terms of quality assessment. Qualitative comparisons based on the visual results shown in Figures 5 and 7 further highlight the advantages of our method. Analysis reveals that the traditional TV-based approaches, including TVℓ_1 and ℓ_0TV, tend to produce noticeable staircase artifacts in smooth regions, which is a well-known limitation of TV regularization. The TVℓ_1 model exhibits significant performance degradation under high-noise conditions. As shown in (b3) of Figures 5 and 7, the restored images appear blurry and distorted, particularly in edge and texture regions. While the ℓ_0OTV method demonstrates some improvement in reducing the staircase artifacts, its restoration capability deteriorates considerably as the noise intensity increases. In contrast, the proposed method effectively prevents the staircase effect while preserving sharp edges in all test images, resulting in superior restoration quality.

4.4. Salt-and-pepper noise and blur removal in color images

In this experiment, we specifically aimed to evaluate the efficacy of the proposed algorithm for restoring color images. To this end, we selected the images *Bird* and *Monarch* as our test subjects. The test images are degraded by disk blur and salt-and-pepper noise at the levels of 30%, 50%, and 70%. The degradation results are shown in (a1)–(a3) of Figures 8 and 9. It is important to note that all parameters of the proposed method are configured within the specified ranges mentioned earlier to ensure the optimal restoration outcomes. The corresponding reconstruction results are presented in columns 2 to 5 of Figures 8 and 9. For a more comprehensive and quantitative evaluation, we consider the performance metrics of four methods, which include the number of iterations, CPU time, PSNR, SSIM, and LPIPS values. These metrics are summarized in Table 3, providing a clear and concise comparison of the performance via four methods. It is worth noting that we adopt the channel-wise TV for a color image $u = (u_r, u_g, u_b)$, calculate TV independently for each color channel, and then sum them up, namely, $TV_{\text{channel}}(u) = \sum_{i\in\{r,g,b\}} \int_\Omega |\nabla u_i|\, dx$.

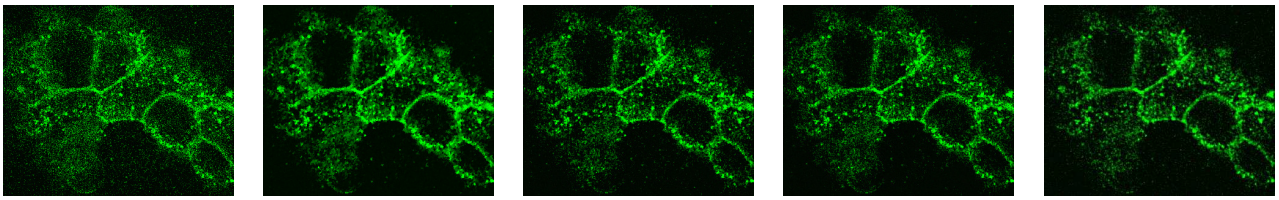

(a) (b) (c) (d) (e)

Figure 10. Real-data denoising results of color fluorescence microscopy image. (a) Real noise image, (b) TVℓ_1, (c) ℓ_0TV, (d) ℓ_0OTV, (e) our method.

The experimental results confirm that the proposed method demonstrates significant advantages in

color image restoration. Visual inspection of Figures 8 and 9 reveals that the TVℓ_1 method introduces noticeable staircase artifacts in the restored images, leading to suboptimal visual quality. This issue is particularly pronounced under 70% salt-and-pepper noise, where the method fails to preserve image features effectively, such as the wings of *Monarch* (Figure 9(b3)). Both the ℓ_0TV and ℓ_0OTV models perform better in edge preservation and noise suppression, but they still have some limitations. Specifically, the ℓ_0TV-based model suffers from a significant staircase effect caused by the TV regularization. On the other hand, the ℓ_0OTV model partially reduces this defect but still fails to achieve high restoration quality. The proposed method effectively eliminates the staircase artifacts through the joint optimization of nonconvex HOTV and nonconvex ℓ_0 norm fidelity terms, while also excelling in detail preservation, as clearly shown in (e1)–(e4) of Figures 8 and 9. Furthermore, quantitative results in Table 3 highlight the superiority of the proposed method, achieving the highest PSNR and SSIM values and demonstrating its exceptional performance in image denoising and deblurring.

4.5. Real-data denoising experiment

Finally, we assessed the effectiveness of our approach to the real-world data experiment. The real fluorescence microscopy image was acquired from the Imaging Center of the IGBMC, Illkirch, France. The input noisy image has the size of 378×313 pixels. After the restoration, Figure 10 presents the visual outputs obtained by using four different methods.

The experimental findings indicate that both the comparative denoising techniques and our newly proposed method are capable of effectively mitigating noise in real-world noisy images. As depicted in Figure 10, our strategy exhibits enhanced performance, resulting in superior denoising effects, which are reflected in terms of noise reduction and detail preservation.

5. Conclusions

This paper introduced a novel nonconvex variational framework designed for high-quality image restoration under blur and impulse noise. The proposed method leveraged the strengths of nonconvex high-order total variation regularization and ℓ_0 norm data fidelity, enabling high-precision image recovery. To solve the designed optimization problem, we developed a modified alternating direction method of multipliers by incorporating the variable splitting method and the iteratively reweighted ℓ_1 algorithm. Experimental results validated that the proposed method outperforms some existing methods in terms of both quantitative metrics and perceptual quality. Moreover, by adjusting the data fidelity term, the framework has the potential for broader applications in denoising tasks involving diverse noise distributions. Furthermore, inspired by periodic plus smooth image decomposition [31], our proposed method can be improved to a more precise algorithm, which helps to overcome the periodization artifacts and preserve edge details.

Use of AI tools declaration

The authors declare they have not used Artificial Intelligence (AI) tools in the creation of this article.

Acknowledgments

This work was supported by the Guangxi Natural Science Foundation (2025GXNSFAA069860), the Scientific Research Fund of Hunan Provincial Education Department (22A0339), and the Guangxi Minzu University Autonomous Regional-Level College Students' Innovation and Entrepreneurship Training Program (S202410608006).

Conflict of interest

The authors declare there are no conflicts of interest.

References

1. T. Shongwe, A. J. H. Vinck, H. C. Ferreira, A study on impulse noise and its models, *SAIEE Afr. Res. J.*, **106** (2015), 119–131. https://doi.org/10.23919/SAIEE.2015.8531938
2. B. Jahne, *Digital Image Processing*, Springer Science, Business Media, 2005. https://doi.org/10.1007/3-540-27563-0
3. L. I. Rudin, S. Osher, E. Fatemi, Nonlinear total variation based noise removal algorithms, *Physica D*, **60** (1992), 259–268. https://doi.org/10.1016/0167-2789(92)90242-F
4. M. Nikolova, Minimizeers of cost-functions involving non-smooth data fidelity terms. Application to the processing of outliers, *SIAM J. Numer. Anal.*, **40** (2002), 965–994. https://doi.org/10.2307/4100911
5. J. Yang, Y. Zhang, W. Yin, An efficient TVL1 algorithm for deblurring multichannel images corrupted by impulsive noise, *SIAM J. Sci. Comput.*, **31** (2009), 2842–2865. https://doi.org/10.1137/080732894
6. T. Chan, A. Marquina, P. Mulet, High-order total variation-based image restoration, *SIAM J. Sci. Comput.*, **22** (2000), 503–516. https://doi.org/10.1137/S1064827598344169
7. K. Bredies, M. Holler, Higher-order total variation approaches and generalisations, *Inverse Probl.*, **36** (2020), 123001. https://doi.org/10.1088/1361-6420/ab8f80
8. M. Bergounioux, L. Piffet, A second-order model for image denoising, *Set-Valued Var. Anal.*, **18** (2010), 277–306. https://doi.org/10.1007/s11228-010-0156-6
9. K. Bredies, K. Kunisch, T. Pock, Total generalized variation, *SIAM J. Imaging Sci.*, **3** (2010), 492–526. https://doi.org/10.1137/090769521
10. X. Liu, Augmented Lagrangian method for total generalized variation based Poissonian image restoration, *Comput. Math. Appl.*, **71** (2016), 1694–1705. https://doi.org/10.1016/j.camwa.2016.03.005
11. H. Deng, G. Liu, L. Zhou, Ultrasonic logging image denoising algorithm based on variational Bayesian and sparse prior, *J. Electron. Imaging*, **32** (2023), 013004–013004. https://doi.org/10.1117/1.JEI.32.1.013004
12. L. Zhou, J. Tang, Fraction-order total variation blind image restoration based on L1-norm, *Appl. Math. Model.*, **51** (2017), 469–476. https://doi.org/10.1016/j.apm.2017.07.009

13. L. Zhou, T. Zhang, Y. Tian, H. Huang, Fraction-order total variation image blind restoration based on self-similarity features, *IEEE Access*, **8** (2020), 30436–30444. https://doi.org/10.1109/ACCESS.2020.2972269

14. M. Nikolova, M. K. Ng, C. P. Tam, Fast nonconvex nonsmooth minimization methods for image restoration and reconstruction, *IEEE Trans. Image Process.*, **19** (2010), 3073–3088. https://doi.org/10.1109/TIP.2010.2052275

15. P. Ochs, A. Dosovitskiy, T. Brox, T. Pock, On iteratively reweighted algorithms for nonsmooth nonconvex optimization, *SIAM J. Imaging Sci.*, **8** (2015), 331–372. https://doi.org/10.1137/140971518

16. M. Nikolova, M. K. Ng, C. P. Tam, On ℓ_1 data fitting and concave regularization for image recovery, *SIAM J. Sci. Comput.*, **35** (2013), A397–A430. https://doi.org/10.1137/10080172X

17. I. Selesnick, A. Lanza, S. Morigi, F. Sgallari, Non-convex total variation regularization for convex denoising of signals, *J. Math. Imaging Vis.*, **62** (2020), 825–841. https://doi.org/10.1007/s10851-019-00937-5

18. X. You, N. Cao, W. Wang, An MTL1TV non-convex regularization model for MR image reconstruction using the alternating direction method of multipliers, *Electron. Res. Arch.*, **32** (2024), 3433–3456. https://doi.org/10.3934/era.2024159

19. X. Liu, W. Lian, Non-convex high-order TV and ℓ_0-norm wavelet frame-based speckle noise reduction, *IEEE Trans. Circuits Syst. II, Exp. Briefs.*, **69** (2022), 5174–5178. https://doi.org/10.1109/TCSII.2022.3197237

20. T. Adam, R. Paramesran, K. Ratnavelu, A combined higher order non-convex total variation with overlapping group sparsity for Poisson noise removal, *Comput. Appl. Math.*, **41** (2022), 130. https://doi.org/10.1007/s11042-021-10583-y

21. X. Liu, T. Sun, Hybrid non-convex regularizers model for removing multiplicative noise, *Comput. Math. Appl.*, **126** (2022), 182–195. https://doi.org/10.1016/j.camwa.2022.09.012

22. W. Lian, X. Liu, Non-convex fractional-order TV model for impulse noise removal, *J. Comput. Appl. Math.*, **417** (2023), 114615. https://doi.org/10.1016/j.cam.2022.114615

23. L. Bai, A new nonconvex approach for image restoration with Gamma noise, *Comput. Math. Appl.*, **77** (2019), 2627–2639. https://doi.org/10.1016/j.camwa.2018.12.045

24. H. Na, M. Kang, M. Jung, M. Kang, Nonconvex TGV regularization model for multiplicative noise removal with spatially varying parameters, *Inverse Probl. Imaging*, **13** (2019), 117–147. https://doi.org/10.3934/ipi.2019007

25. T. Sun, X. Liu, Non-convex TGV regularized ℓ_0-norm fidelity model for impulse noise removal, *Signal Process.*, **212** (2023), 109125. https://doi.org/10.1016/j.sigpro.2023.109125

26. S. Kuang, H. Chao, Q. Li, Matrix completion with capped nuclear norm via majorized proximal minimization, *Neurocomputing*, **316** (2018), 190–201. https://doi.org/10.1016/j.neucom.2018.07.066

27. G. Yuan, B. Ghanem, ℓ_0TV: A sparse optimization method for impulse noise image restoration, *IEEE Trans. Pattern Anal. Mach. Intell.*, **41** (2017), 352–364. https://doi.org/10.1109/TPAMI.2017.2783936

28. H. Attouch, J. Bolte, B. F. Svaiter, Convergence of descent methods for semi-algebraic and tame problems: proximal algorithms, forward-backward splitting, and regularized Gauss-Seidel methods, *Math. Program.*, **137** (2013), 91–129. https://doi.org/10.1007/s10107-011-0484-9

29. J. Bolte, S. Sabach, M. Teboulle, Proximal alternating linearized minimization for nonconvex and nonsmooth problems, *Math. Program.*, **146** (2014), 459–494. https://doi.org/10.1007/s10107-013-0701-9

30. M. Yin, T. Adam, R. Paramesran, M. F. Hassan, An ℓ_0-overlapping group sparse total variation for impulse noise image restoration, *Signal Process., Image Commun.*, **102** (2022), 116620. https://doi.org/10.1016/j.image.2021.116620

31. L. Moisan, Periodic plus smooth image decomposition, *J. Math. Imaging Vis.*, **39** (2011) 161–179. https://doi.org/10.1007/s10851-010-0227-1

AIMS Press